Diffusion Experiments with a Global Discontinuous Galerkin Shallow-Water Model

RAMACHANDRAN D. NAIR

Computational Mathematics Group, Institute for Mathematics Applied to Geosciences (IMAGe), National Center for Atmospheric Research, Boulder, Colorado*

(Manuscript received 28 October 2008, in final form 13 March 2009)

ABSTRACT

A second-order diffusion scheme is developed for the discontinuous Galerkin (DG) global shallow-water model. The shallow-water equations are discretized on the cubed sphere tiled with quadrilateral elements relying on a nonorthogonal curvilinear coordinate system. In the viscous shallow-water model the diffusion terms (viscous fluxes) are approximated with two different approaches: 1) the element-wise localized discretization without considering the interelement contributions and 2) the discretization based on the local discontinuous Galerkin (LDG) method. In the LDG formulation the advection–diffusion equation is solved as a first-order system. All of the curvature terms resulting from the cubed-sphere geometry are incorporated into the first-order system. The effectiveness of each diffusion scheme is studied using the standard shallow-water test cases. The approach of element-wise localized discretization of the diffusion term is easy to implement but found to be less effective, and with relatively high diffusion coefficients, it can adversely affect the solution. The shallow-water tests show that the LDG scheme converges monotonically and that the rate of convergence is dependent on the coefficient of diffusion. Also the LDG scheme successfully eliminates small-scale noise, and the simulated results are smooth and comparable to the reference solution.

1. Introduction

Diffusion and dissipation mechanisms play an important role in atmospheric modeling. In a discrete climate model, momentum diffusion transfers energy from the resolved scales into the unresolved scales. Horizontal diffusion parameterizes the energy transfer from wave disturbances into the unresolved scales, preventing spurious accumulation of energy and enstrophy at the model grid scale. The importance of diffusivity in atmospheric modeling was recognized in the early model development, which paved the way for pioneering research in this field (e.g., Smagorinsky 1963; Leith 1971). A theoretical account of the diffusion mechanisms in geophysical fluid dynamics is provided in textbooks by Pedlosky (1987) and Durran (1999).

The design of the diffusion scheme is primarily based on the model's spatial discretization. There are various approaches to invoke diffusivity in atmospheric models, out of which the second-order explicit diffusion (∇^2) seems to be the most common. High-order hyperdiffusion or hyperviscosity (∇^{2n}, $n = 2, 3, \ldots$) is employed in spectral transform–based models. For example, the climate model developed (Collins et al. 2004) at the National Center for Atmospheric Research (NCAR) relies on hyperdiffusion. Burkhardt and Becker (2006) discuss the lack of angular momentum conservation with hyperdiffusion and the development of consistent ∇^2 diffusion, which addresses conservation issues. Gelb and Gleeson (2001) developed a spectral viscosity method as an alternative for the horizontal diffusion in a global shallow-water model. Recently, Taylor et al. (2007) successfully implemented hyperdiffusion (∇^4) in a spectral element–based dynamical core [this is an integral part of the High-Order Method Modeling Framework (HOMME) developed at the NCAR].

In this paper we focus on the implementation of second-order diffusion in the discontinuous Galerkin (DG) shallow-water model developed by Nair et al. (2005a, hereinafter NTL05a) on the cubed sphere. The DG method is gaining prominence in both hydrostatic

* The National Center for Atmospheric Research is sponsored by the National Science Foundation.

Corresponding author address: Ramachandran D. Nair, National Center for Atmospheric Research, IMAGe, 1850 Table Mesa Dr., Boulder, CO 80305.
E-mail: rnair@ucar.edu

DOI: 10.1175/2009MWR2843.1

(HOMME-DG dynamical core; Nair and Tufo 2007; Nair et al. 2009) and nonhydrostatic (Giraldo and Restelli 2008) atmospheric modeling, primarily due to the inherent conservation properties and parallel scalability (efficiency) of DG algorithms (Cockburn and Shu 2001). In a seminal work Bassi and Rebay (1997, hereinafter BR97) introduced explicit diffusion (viscous flux) in the DG discretization for solving compressible Navier–Stokes equations. Cockburn and Shu (1998) laid a rigorous mathematical background to this approach and generalized it to the so-called local DG (LDG) method. The LDG method is not limited to the advection–diffusion problem (Dawson and Aizinger 2002); rather it is applicable to a class of elliptic problems (Arnold et al. 2002). Here we only focus on the diffusion problem closely following BR97 and treating it as a special case of LDG. The nonorthogonal curvilinear coordinates associated with the cubed-sphere geometry make the LDG implementation for the shallow-water model more challenging as we will discuss in this paper.

In section 2, we briefly review the shallow-water model and introduce basic notations. The DG discretization of the viscous shallow-water model based on LDG approach and its implementation on the cubed sphere are discussed in section 3, followed by numerical experiments in section 4. Section 5 provides the summary and conclusions.

2. The shallow-water model on the cubed sphere

The physical domain is a sphere $\mathcal{S}$, representing the planet Earth, based on the cubed-sphere topology originally introduced by Sadourny (1972). Here we consider the cubed-sphere geometry employing the equiangular central projection as described in Nair et al. (2005b). The cubed-sphere geometry consists of partitioning $\mathcal{S}$ into six identical regions that are obtained by the central projection of the faces of the inscribed cube onto the surface of $\mathcal{S}$. Each of the local coordinate systems is free of singularities, employs identical metric terms, and creates a nonorthogonal curvilinear coordinate system on $\mathcal{S}$. However, the edges of the faces are discontinuous. The local coordinates (or central angles of the projection) for each face are $x^1 = x^1(\lambda, \theta)$, $x^2 = x^2(\lambda, \theta)$ such that $x^1, x^2 \in [-\pi/4, \pi/4]$, where λ and θ are the longitude and latitude, respectively, of a sphere with radius R. The metric tensor G_{ij} associated with the transformation is

$$G_{ij} = \frac{R^2}{\rho^4 \cos^2 x^1 \cos^2 x^2} \begin{bmatrix} 1 + \tan^2 x^1 & -\tan x^1 \tan x^2 \\ -\tan x^1 \tan x^2 & 1 + \tan^2 x^2 \end{bmatrix},$$

where $i, j \in \{1, 2\}$ and $\rho^2 = 1 + \tan^2 x^1 + \tan^2 x^2$. The Jacobian of the transformation (the metric term) is $\sqrt{G} = [\det(G_{ij})]^{1/2}$.

The flux form shallow-water (SW) model developed on the cubed sphere by NTL05a relies on nonorthogonal curvilinear coordinates. In the present work we extend this model to a viscous SW model. The SW equations are treated in tensorial form with covariant (u_i) and contravariant (u^i) wind vectors, which are related through $u_i = G_{ij}u^j$, $u^i = G^{ij}u_j$, and $G^{ij} = G_{ij}^{-1}$. The orthogonal components of the spherical wind vector $\mathbf{v}(\lambda, \theta) = (u, v)$ can be expressed in terms of contravariant vectors (u^1, u^2) as follows:

$$\begin{bmatrix} u \\ v \end{bmatrix} = \mathbf{A} \begin{bmatrix} u^1 \\ u^2 \end{bmatrix},$$

$$\mathbf{A} = \begin{bmatrix} R\cos\theta\partial\lambda/\partial x^1 & R\cos\theta\partial\lambda/\partial x^2 \\ R\partial\theta/\partial x^1 & R\partial\theta/\partial x^2 \end{bmatrix}; \quad \mathbf{A}^{\mathrm{T}}\mathbf{A} = G_{ij}.$$

The details of the local transformation laws and $\mathbf{A}$ for each face of the cubed sphere can be found in Nair et al. (2005b).

a. The viscous SW equations

The governing equations for viscous flow of a thin layer of fluid in 2D are the horizontal momentum and continuity equations for the height h. Here, h is the depth of the fluid and it is related to the free surface geopotential height (above sea level) $\Phi = g(h_s + h)$, where h_s denotes the height of the underlying mountains and g is the gravitational acceleration. The momentum equations are cast in covariant (u_1, u_2) form, which are analogous to the vector-invariant formulation as given in Williamson et al. (1992, hereinafter W92). Thus, the prognostic variables are u_1, u_2, and h, and the shallow-water equations on $\mathcal{S}$ can be written in a compact form following the inviscid formulation in NTL05a:

$$\frac{\partial}{\partial t}\mathbf{U} + \frac{\partial}{\partial x^1}\mathbf{F}_1(\mathbf{U}) + \frac{\partial}{\partial x^2}\mathbf{F}_2(\mathbf{U}) = \mathbf{S}(\mathbf{U}) + \mathbf{D}(\mathbf{U}), \tag{1}$$

where the state vector $\mathbf{U}$ and the flux vectors $\mathbf{F}_1$ and $\mathbf{F}_2$ are defined by

$$\mathbf{U} = [u_1, u_2, \sqrt{G}h]^{\mathrm{T}}, \quad \mathbf{F}_1 = [E, 0, \sqrt{G}hu^1]^{\mathrm{T}}, \quad \text{and}$$
$$\mathbf{F}_2 = [0, E, \sqrt{G}hu^2]^{\mathrm{T}},$$

where $E = \Phi + \frac{1}{2}(u_1u^1 + u_2u^2)$ is the energy term. The divergence δ and relative vorticity ζ on $\mathcal{S}$ are defined as

$$\delta = \frac{1}{\sqrt{G}}\left[\frac{\partial\sqrt{G}u^1}{\partial x^1} + \frac{\partial\sqrt{G}u^2}{\partial x^2}\right] \quad \text{and} \quad \zeta = \frac{1}{\sqrt{G}}\left[\frac{\partial u_2}{\partial x^1} - \frac{\partial u_1}{\partial x^2}\right]. \tag{2}$$

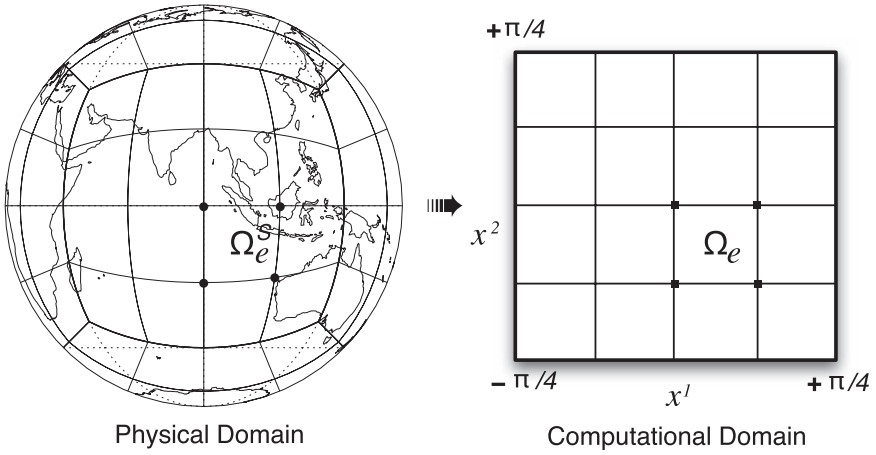

FIG. 1. A schematic diagram showing the facewise mapping between the cubed sphere $\mathcal{S}$ (physical domain) and the cube $\mathcal{C}$ (computational domain) such that there exists a one-to-one correspondence between the spherical element Ω_e^S on $\mathcal{S}$ and the planar element Ω_e on $\mathcal{C}$. Each face of the cube has $N_e \times N_e$ elements ($N_e = 4$) defined by local computational coordinates (x^1, x^2) with $x^1, x^2 \in [-\pi/4, \pi/4]$.

The source term $\mathbf{S}$ is a function of relative vorticity ζ, Coriolis term f, and contravariant wind vector (u^1, u^2), and is defined as

$$\mathbf{S}(\mathbf{U}) = [\sqrt{G}u^2(f+\zeta), -\sqrt{G}u^1(f+\zeta), 0]^{\mathrm{T}}.$$

In (1), $\mathbf{D}(\mathbf{U})$ represents the viscous flux that is formally defined to be

$$\mathbf{D}(\mathbf{U}) = \mathbf{D}_\nu \sqrt{G}\nabla_s^2(\mathbf{U}), \quad \mathbf{D}_\nu = \begin{bmatrix} \nu & 0 & 0 \\ 0 & \nu & 0 \\ 0 & 0 & 0 \end{bmatrix},$$

where $\mathbf{D}_\nu$ is the diffusive flux matrix with the coefficient of diffusion ν and ∇_s^2 is the Laplacian operator defined on $\mathcal{S}$. Since we consider the application of uniform diffusion to the momentum equations in (1), $\mathbf{D}(\mathbf{U})$ can be written in the following simple form:

$$\mathbf{D}(\mathbf{U}) = [\nu\sqrt{G}\nabla_s^2 u_1, \nu\sqrt{G}\nabla_s^2 u_2, 0]^{\mathrm{T}}.$$

For an arbitrary variable U, the Laplacian terms in the above equation can be written in the following explicit form:

$$\begin{aligned}\sqrt{G}\nabla_s^2 U &\equiv \sqrt{G}\,\mathrm{div}[\mathrm{grad}(U)] \\ &= \frac{\partial}{\partial x^1}\left[\sqrt{G}G^{11}\frac{\partial U}{\partial x^1} + \sqrt{G}G^{12}\frac{\partial U}{\partial x^2}\right] \\ &\quad + \frac{\partial}{\partial x^2}\left[\sqrt{G}G^{21}\frac{\partial U}{\partial x^1} + \sqrt{G}G^{22}\frac{\partial U}{\partial x^2}\right].\end{aligned} \tag{3}$$

Note that here the Laplacian is applied component wise for each momentum equation, and for simplicity the general vector Laplacian is not considered. In curvilinear coordinates the vector Laplacian is different from the Laplacian of the components.

b. The computational domain

The spherical SW equations can be discretized either in the physical space or in the computational (transformed) space. By the virtue of central projections the SW equations in (1) are already in the computational (x^1, x^2) space. Therefore, it is convenient discretize the system in (1) in the same space. The computational domain may be considered as a logical cube $\mathcal{C} \subset \mathbb{R}^2$ such that each face of $\mathcal{C}$ is defined in terms of local orthogonal Cartesian coordinates (x^1, x^2), where $x^1, x^2 \in [-\pi/4, \pi/4]$. Thus, $\mathcal{C}$ is essentially a union of six nonoverlapping subdomains (faces) and any point on $\mathcal{C}$ can be uniquely represented by the ordered triple (x^1, x^2, p), where $p = 1, \ldots, 6$, is the cube face (panel) index as shown in Fig. 2 of Nair et al. (2005b). The equiangular central projection results in a uniform element width ($\Delta x^1 = \Delta x^2$) on $\mathcal{C}$, which is an advantage for practical implementation. Figure 1 illustrates a schematic diagram of the mapping between the physical domain $\mathcal{S}$ (cubed sphere) and the computational domain $\mathcal{C}$ (cube).

A salient feature of the cubed-sphere geometry is that $\mathcal{S}$ is naturally decomposed into nonoverlapping quadrilateral elements (tiles) Ω_e^S. This topology is well suited to high-order element-based methods such as DG. Each face of the cubed sphere has $N_e \times N_e$ elements, thus $6N_e^2 = N_{\mathrm{elem}}$ elements span the entire spherical domain

such that $\mathcal{S} = \cup_{e=1}^{N_{\text{elem}}} \Omega_e^S$, and in Fig. 1 N_e is set to 4. Note that, there exists a one-to-one correspondence between spherical element Ω_e^S on $\mathcal{S}$ and planar element Ω_e on $\mathcal{C}$. The integral and the differential operators required in the DG discretization of SW system can be approximated on each Ω_e with boundary Γ_e.

For simplicity, we consider a generic component of the system (1) as follows:

$$\frac{\partial}{\partial t} U + \nabla_c \cdot \mathbf{F}(U) = \nu \sqrt{G} \nabla_s^2 U + S(U), \quad \text{in} \quad \mathcal{C} \times (0, T], \tag{4}$$

where $\mathbf{F} = (F_1, F_2)$ is the flux function, T is the prescribed time, and $\nabla_c \equiv (\partial/\partial x^1, \partial/\partial x^2)$ is the gradient operator in (x^1, x^2) space such that $\nabla_c \cdot \mathbf{F} = \partial F_1/\partial x^1 + \partial F_2/\partial x^2$. The DG discretization of (1) will be described in terms of (4) in the following section.

3. DG discretization

a. Weak formulation

We first introduce some basic notations required for the discretization. Let $\mathcal{V}_h$ be a finite-dimensional space of polynomials of degree up to N such that

$$\mathcal{V}_h = \{\varphi \in L^2(\mathcal{C}) : \varphi|_{\Omega e} \in \mathcal{P}_N(\Omega_e), \quad \forall \quad \Omega_e \in \mathcal{C}\}, \tag{5}$$

where

$$\mathcal{P}_N = \text{span}\{(x^1)^m (x^2)^n : 0 \le m, \quad n \le N\}.$$

The weak formulation of the problem can be obtained by multiplying (4) by a test function and integrating by parts over $\mathcal{C}$ (Cockburn and Shu 2001). To find the approximate solution $U_h \in \mathcal{V}_h$ we consider the following semidiscretized weak formulation on each element Ω_e such that

$$\frac{d}{dt}\int_{\Omega_e} U_h \varphi_h \, d\Omega - \int_{\Omega_e} \mathbf{F}(U_h) \cdot \nabla_c \varphi_h \, d\Omega + \int_{\Gamma_e} \hat{\mathbf{F}} \cdot \mathbf{n} \varphi_h \, d\Gamma = \nu \int_{\Omega_e} \sqrt{G} \nabla_s^2 U_h \varphi_h \, d\Omega + \int_{\Omega_e} S(U_h) \varphi_h \, d\Omega, \tag{6}$$

where φ_h is a test function in $\mathcal{V}_h$, $\hat{\mathbf{F}}$ is the numerical flux, $\mathbf{n}$ is the outward-facing unit normal vector on the element boundary Γ_e, and the element of integration is $d\Omega = dx^1 dx^2$. There are several choices for numerical flux schemes. However, for the present study we employ the local Lax–Friedrichs numerical flux as follows:

$$\hat{\mathbf{F}}(U_h) = \frac{1}{2}\{[\mathbf{F}(U_h^-) + \mathbf{F}(U_h^+)] - \alpha(U_h^+ - U_h^-)\}, \tag{7}$$

where α is the maximum of the eigenvalues of the flux Jacobian (NTL05a); U_h^- and U_h^+, respectively, are the left and right limits of U_h along the boundary Γ_e such that U_h^- is interior to the element Ω_e and U_h^+ is in the adjacent neighboring element.

Except for the viscous flux term, the evaluations of the integrals in (6) can be performed as in the case of inviscid SW model, but the discretization of the viscous flux term requires special attention. An obvious option is the direct discretization of the diffusion operator locally over each Ω_e such that

$$(\nabla_s^2 U_h)\big|_{\Omega_e} = \nabla_s^2 (U_h\big|_{\Omega e}), \tag{8}$$

where the interelemental contributions of U_h (e.g., gradient information) across the boundary Γ_e are ignored. Such localized computations are desirable for parallel implementation because no additional communication between the elements is required for the SW code and the computational overheads are local to the element. Note that for modern high-performance computers, the parallel communication between the processors is often an order more expensive than localized computation.

Despite the computational advantages, the element-wise localized diffusion operation based on (8) has some serious limitations. Diffusivity is a physical entity and its artificial localized *blocking* via (8) in the integration of (6) may have adverse effects on the diffusion mechanism in the viscous SW model. In some literature such element-wise localized diffusion, which does not take interelement contributions into account, is referred to as the inconsistent DG formulation for diffusion (Karniadakis and Sherwin 2005). In Persson and Peraire (2006) it is mentioned that such approaches tend to flatten the solution within each element and increases the interelement jumps. However, we consider the "element-wise localized diffusion without interelement contributions" (or ELD) for a standard SW test case and demonstrate the results in section 4. This is just to see how effective the ELD approach is as a diffusion operation.

b. The LDG formulation

Implementation of the LDG scheme for the SW system in (1) follows the same principle laid by BR97. Nevertheless, the curvilinear gradients and Laplacians need special treatment. The key idea of the LDG approach is to introduce a local auxiliary variable for the gradient and rewrite the (4) as a first-order system. This is required because the high-order derivatives involved

in diffusive fluxes in SW system are not amenable to the regular DG discretization.

For the generic component (4) of the SW system, consider the auxiliary variable $\mathbf{q} = \nabla_c U$, and recast the spherical Laplacian ∇_s^2 in terms of gradient operator ∇_c defined on $\mathcal{C}$. The following matrix notations are used for representing $\nabla_s^2 U$ in the LDG formulation:

$$\mathbf{q} = \left[\frac{\partial U}{\partial x^1}, \frac{\partial U}{\partial x^2}\right], \quad \mathbf{M} = \begin{bmatrix} \sqrt{G}G^{11} & \sqrt{G}G^{12} \\ \sqrt{G}G^{21} & \sqrt{G}G^{22} \end{bmatrix}, \quad \text{and}$$

$$\tilde{\mathbf{q}} = \mathbf{q}\mathbf{M}^{\mathrm{T}}.$$

With these notations, the spherical Laplacian introduced in (3) can be expressed in a compact form:

$$\sqrt{G}\nabla_s^2 U = \nabla_c \cdot \tilde{\mathbf{q}}, \tag{9}$$

and (4) can be written as a first-order system on $\mathcal{C}$:

$$\mathbf{q} - \nabla_c U = 0, \tag{10}$$

$$\tilde{\mathbf{q}} = \mathbf{q}\mathbf{M}^{\mathrm{T}}, \quad \text{and} \tag{11}$$

$$\frac{\partial U}{\partial t} + \nabla_c \cdot \mathbf{F}(U) - \nu \nabla_c \cdot \tilde{\mathbf{q}} = S(U). \tag{12}$$

A weak formulation corresponding to (10) for an approximate solution $U_h \in \mathcal{V}_h$ with $\mathbf{q}_h = \nabla_c U_h$, can be obtained by multiplying (10) by a vector test function w and integrating by parts. On each element Ω_e with boundary Γ_e on $\mathcal{C}$, the weak form results in

$$\int_{\Omega_e} \mathbf{q}_h \cdot \mathbf{w}\, d\Omega = \int_{\Gamma_e} U_h \mathbf{w} \cdot \mathbf{n}\, d\Gamma - \int_{\Omega_e} U_h \nabla_c \cdot \mathbf{w}\, d\Omega, \tag{13}$$

where each component of $\mathbf{w}$ belongs to $\mathcal{V}_h$. If the flux associated with U_h along the boundary Γ_e is approximated by the central flux (BR97):

$$[U_h] \equiv \frac{1}{2}(U_h^+ + U_h^-) = \frac{1}{2}(U_h^+ - U_h^-) + U_h^-,$$

then integrating the last term in (13) by parts (Green's method) leads to

$$\int_{\Omega_e} \mathbf{q}_h \cdot \mathbf{w}\, d\Omega = \int_{\Gamma_e} \frac{1}{2}(U_h^+ - U_h^-)\mathbf{w} \cdot \mathbf{n}\, d\Gamma + \int_{\Omega_e} \nabla_c U_h \cdot \mathbf{w}\, d\Omega, \tag{14}$$

where the numerical flux $(U_h^+ - U_h^-)/2$ is referred to as the jump flux. The semidiscretized weak formulation corresponding to (12), with the diffusion term (viscous flux) $\tilde{\mathbf{q}}_h = \mathbf{q}_h \mathbf{M}^{\mathrm{T}}$, becomes

$$\frac{d}{dt}\int_{\Omega_e} U_h \varphi_h\, d\Omega - \int_{\Omega_e} \mathbf{F}(U_h) \cdot \nabla_c \varphi_h\, d\Omega + \int_{\Gamma_e} \hat{\mathbf{F}} \cdot \mathbf{n}\varphi_h\, d\Gamma + \nu\left(\int_{\Omega_e} \tilde{\mathbf{q}}_h \cdot \nabla_c \varphi_h\, d\Omega - \int_{\Gamma_e} [\tilde{\mathbf{q}}_h] \cdot \mathbf{n}\varphi_h\, d\Gamma\right) = \int_{\Omega_e} S(U_h)\varphi_h\, d\Omega, \tag{15}$$

where $[\tilde{\mathbf{q}}_h]$ is the central flux $(\tilde{\mathbf{q}}_h^+ + \tilde{\mathbf{q}}_h^-)/2$ and $\hat{\mathbf{F}}$ is the numerical flux (7). Note that the term $\tilde{\mathbf{q}}_h = \mathbf{q}_h \mathbf{M}^{\mathrm{T}}$ in (15) is computed after finding the gradient q_h using (14).

Because of the simplicity, in this study we are particularly interested in the jump flux and central flux combinations for (13) and (15), respectively, as described in BR97. However, a variety of choices are available for the numerical fluxes, with varying complexity, as needed in the discrete weak formulations in (13) and (15). A comprehensive list of numerical fluxes used for the LDG method is given in Arnold et al. (2002). The theoretical study by Arnold et al. (2002) suggests that the central flux formulation (BR97) may lead to a weakly stable scheme, but that did not occur in the numerical experiments considered in section 4.

c. Numerical integration

Now we describe the evaluations of the discretized weak formulations in (6), (13), and (15). An important aspect of the DG discretization is the choice of an appropriate set of basis functions (polynomials) that span $\mathcal{V}_h$. To evaluate the integrals in the weak formulations efficiently and accurately, an orthogonal polynomial based basis set is usually employed. Recently Levy et al. (2007) showed that, for high-order elements, the nodal DG version is significantly more efficient than the modal version. Here we adopt the nodal basis set as the one used in the HOMME dynamical core (Nair et al. 2009).

To take the advantage of efficient quadrature rules, new independent variables $\xi^i = \xi^i(x^i)$, $i \in \{1, 2\}$ are introduced in such a way that $\xi^i \in [-1, 1]$. This leads to an affine mapping of each element $\Omega_e \in \mathcal{C}$ to a unique reference element $Q = [-1, 1] \otimes [-1, 1]$. The nodal basis functions are the Lagrange–Legendre polynomials $h_\ell(\xi^i)$, with roots at the Gauss–Lobatto quadrature points. These orthogonal basis functions are defined by

$$h_\ell(\xi^i) = \frac{(\xi^i - 1)(\xi^i + 1)L_N'(\xi^i)}{N(N+1)L_N(\xi_\ell)(\xi^i - \xi_\ell)};$$

$$\int_{-1}^{1} h_k(\xi^i)h_\ell(\xi^i)\, d\xi^i \simeq w_k \delta_{k\ell}, \tag{16}$$

where L_N is the Legendre polynomial of degree N, $0 \le k, \ell \le N$; w_k is the weight associated with the

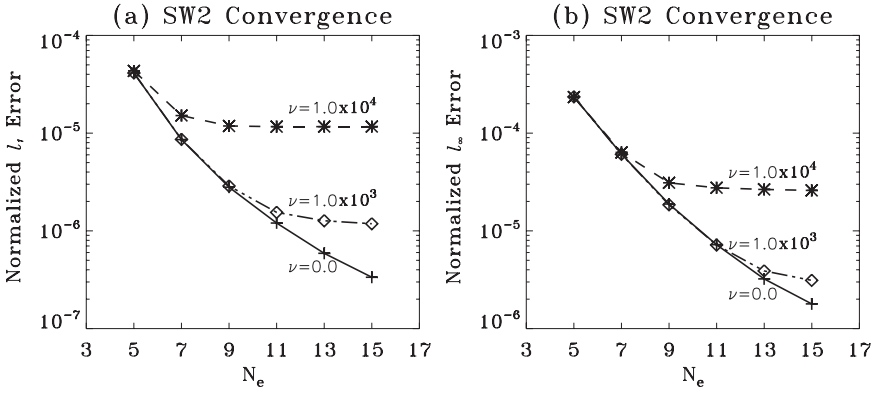

FIG. 2. The normalized standard (a) ℓ_1 and (b) ℓ_∞ height errors as a function of number of elements (N_e) for the test case 2 with the viscous SW model. Third-degree polynomials ($N_v = 4$) are used for DG spatial discretization, and the values of the diffusion coefficient ν (m^2 s^{-1}) in the LDG formulations are 0.0, 1.0×10^3, and 1.0×10^4.

Gauss–Lagendre–Lobatto (GLL) quadrature rule and $\delta_{k\ell}$ is the Kronecker delta function. There are other options for choosing the basis functions and quadrature rules; Karniadakis and Sherwin (2005) provide a detailed account on this topic.

The nodal basis set that spans $\mathcal{P}_N$ in (5) is chosen to be a tensor product of polynomials $h_k(\xi^1)h_\ell(\xi^2)$. Now the approximate solution U_h and test function φ_h in $\mathcal{V}_h$ can be expanded in terms of a tensor product of the Lagrange basis functions, and in the case of U_h:

$$U_h(\xi^1, \xi^2) = \sum_{k=0}^{N}\sum_{l=0}^{N} U_h(\xi_k^1, \xi_l^2)h_k(\xi^1)h_\ell(\xi^2), \quad (17)$$

where $\{\xi_l^i\}_{l=0}^N$ are the GLL quadrature points on the reference element Q. With this setup there are $N_v \times N_v$ GLL points on Q where $N_v = N + 1$; thus, the total degrees of freedom on $\mathcal{C}$ is $6N_e^2N_v^2$. Note that the quadrature rule required for the boundary integrals needs to be one order more accurate than the internal integrals (Cockburn and Shu 2001) to maintain overall accuracy in the DG discretization. Nevertheless, we use the same order GLL quadrature rule for the internal integrals in Ω_e and the boundary flux integrals along Γ_e, because this approach is extremely efficient at the cost of nominal loss of accuracy because of inexact integration (quadrature error).

Substitution of the expansion in (17) for U_h and φ_h in the weak formulations and further simplification leads to the following ordinary differential equation (ODE) in time corresponding to the continuous problem (4):

$$\frac{dU_{k\ell}}{dt} = L(U_{k\ell}) \quad \text{in} \quad (0, T], \quad (18)$$

where $U_{k\ell}$ are the time-dependent nodal (grid point) values corresponding to U_h. For the viscous SW system in (1) a system of ODEs in (18) must be solved for $U_{k\ell}$. In the present study we use a second- or third-order accurate explicit strong stability preserving (SSP) Runge–Kutta (RK) time integration procedure (Gottlieb et al. 2001) for (18).

4. Numerical experiments

To study the impact of diffusion, we consider two test cases from the W92 standard test suite for evaluating SW models on the sphere. These tests are the *steady-state geostrophic flow* and the *flow over an isolated mountain* often referred to as the SW test case 2 and 5, respectively. In addition to that, the barotropic instability test case proposed by Galewsky et al. (2004) is considered. We use the standard normalized ℓ_1 and ℓ_∞ error measures as suggested in W92 for the convergence study.

The explicit RK time integrations are robust and widely used for the DG discretization, even though the resulting scheme has a stringent Courant number restriction. For the element-based high-order methods it is known that the inclusion of diffusion terms further restrict the explicit time stepping (Henderson 1999). Considering these facts for the viscous SW model we employ the second-order SSP RK time integration method combined with a moderate time-step size (suboptimal). The viscous SW model has been implemented in the HOMME framework (Nair et al. 2009), which is highly scalable, and its overall computational expense is dependent on parallel communications. Because of the additional flux computations (parallel communications) needed for the LDG formulation, we found that about

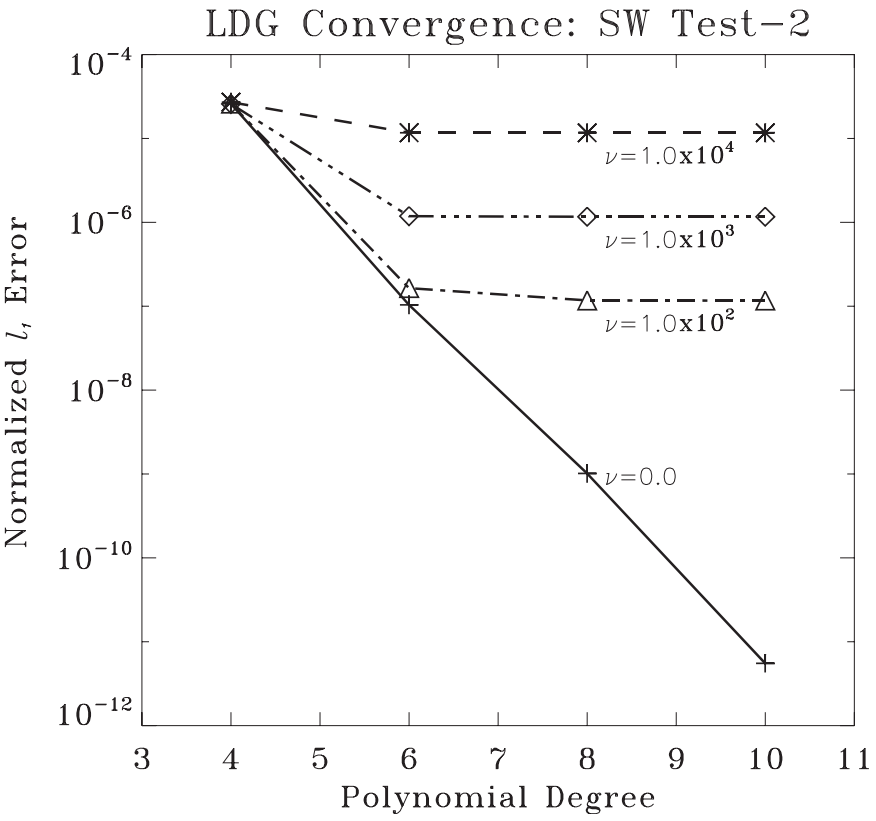

FIG. 3. The normalized standard ℓ_1 height error for test case 2 with different values of the diffusion coefficient ν ($m^2\ s^{-1}$). For this convergence test, the total number of elements are fixed (with $N_e = 3$) and the degree of the polynomial is gradually increased.

30% more computational time was required for the LDG SW model as opposed to the inviscid version. However, the element-wise localized diffusion formulation in (6) does not have the burden of additional parallel communications and requires only 5% more computational time as opposed to the inviscid SW version.

The GLL grid associated with each element results in a highly nonuniform grid on the sphere. Therefore, it is difficult to make a strict comparison of cubed-sphere grid resolution with that of the regular longitude–latitude (λ, θ) grid. However, an *average* resolution at the equator of the cubed sphere may be used for comparing the results (Nair et al. 2009), and is given by the approximate relation $90°/[N_e(N_v - 1)]$. For visualization purpose the numerical results on the cubed-sphere grids is interpolated onto a regular (λ, θ) grid.

a. Steady-state geostrophic flow

First we consider the test case 2, which is a steady-state solution of the full nonlinear shallow-water equations. The wind field is uniform and the equations are geostrophically balanced during the time evolution. The initial velocity and height fields are

$$u = u_0(\cos\alpha_0\ \cos\theta + \sin\alpha_0 \cos\lambda\ \sin\theta),$$
$$v = -u_0 \sin\alpha_0 \sin\lambda, \quad \text{and}$$
$$gh = gh_0 - \frac{u_0}{2}(2aw + u_0) \times (\sin\theta\ \cos\alpha_0 - \cos\lambda \cos\theta\ \sin\alpha_0)^2,$$

where a and ω are the earth's radius and angular velocity, respectively; $u_0 = 2\pi a/(12\ \text{days})$, and $gh_0 = 2.94 \times 10^4\ m^2\ s^{-2}$. The flow orientation parameter α_0 is set to be $\pi/4$, which makes the test more challenging (NTL05a). With these initial conditions the SW model is integrated for 5 model days as recommended in W92. An important feature of this test is that the analytic solution is known at any given time. Therefore, it is convenient to use this test for studying the convergence of SW model.

In high-order element-based numerical models higher model resolutions can be obtained by increasing the number of elements (N_e) or increasing the degree of the polynomials ($N_v - 1$) used for discretization. For the convergence test with test case 2 we employ both options. Figure 2 shows the convergence LDG scheme in terms of ℓ_1 and ℓ_∞ height errors, where the degree of the

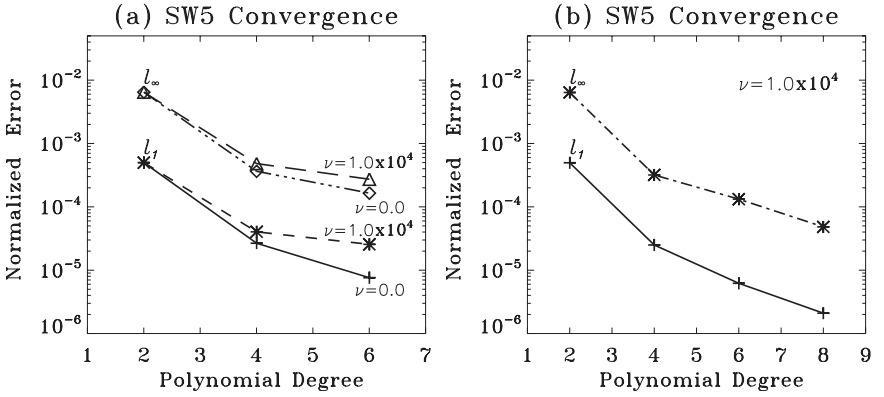

FIG. 4. The normalized standard ℓ_1 and ℓ_∞ height errors for the test case 5 at model day 7. The viscous SW model is integrated while keeping the total number of elements fixed ($N_e = 10$) but with varying polynomial degree. Since no analytic solution is available for this test, a high-order reference solution with an approximate resolution of 1° is computed with the 9th-degree polynomials ($N_v = 10$). (a) The convergence of LDG scheme for height errors where an inviscid reference solution ($\nu = 0.0$) is used. (b) Convergence to a viscid reference solution with $\nu = 1.0 \times 10^4$ m^2 s^{-1}; in this case the same diffusion coefficient is used for all the low-order model integrations.

polynomial is kept to be 3 (i.e., $N_v = 4$) and N_e is increased from 5 to 15. As the model resolution increases, the inviscid version (diffusion coefficient $\nu = 0$) shows *faster* convergence to the exact solution, while the LDG version converges to a ''diffused state'' depending on the value of ν. Similarly Fig. 3 shows the convergence of the height field in terms of ℓ_1 error where $N_e = 3$ but polynomial degree varies from 4 to 10. In this case the inviscid version attains exponential convergence as reported in NTL05a, and for the LDG version convergence is strongly influenced by the magnitude of the diffusion coefficient rather than the polynomial degree. The time step Δt used for the simulations is 180 s except for the combination $N_e = 3, N_v = 11$, where Δt is set to 90 s. Note that in all the cases the LDG SW model converges monotonically to a diffused state that is dependent on ν.

b. Zonal flow over an isolated mountain

This test case is particularly useful for studying the effectiveness of the scheme in conserving integral invariants such as mass, total energy, and potential enstrophy. Gelb and Gleeson (2001) extensively used this test for diffusion experiments in a global spectral model. The ''mountain'' is centered at ($\lambda_c = 3\pi/2, \theta_c = \pi/6$) with height $h_s = 2000(1 - r/a)$ m, where $a = \pi/9$ and $r^2 = \min[a^2, (\lambda - \lambda_c)^2 + (\theta - \theta_c)^2]$. The mean equivalent depth of the atmopshere is set to be $h_0 = 5960$ m. For this test the flow field is highly nonlinear and no analytic solution is available. The initial conditions and other test parameters are described in W92. This test typically causes difficulties for high-order methods such as spectral element and spectral transform methods because of the generation of spurious oscillations (spectral ringing) at all scales. However, despite the high-order spatial spectral representation, the DG model in NTL05a did not exhibit spurious oscillations.

First, we consider the SW test case 5 for a convergence study. No analytic solution is available for this test therefore a ''high resolution'' reference height field is computed with high-order polynomials. The SW model is configured with $N_e = 10$ and $N_v = 10$ (i.e., 9th-degree polynomials) which corresponds to an approximate resolution of 1.0° at the equator, and integrated for 7 model days. The time step Δt used for all the simulations, irrespective of resolution, is 30 s. The convergence results with ℓ_1 and ℓ_∞ height errors are shown in Fig. 4 as a function of the polynomial degree. The convergence plots given in Fig. 4a are based on inviscid reference solution ($\nu = 0.0$ and $N_v = 10$). Figure 4b shows the viscid convergence of the LDG model where the reference solution is computed with $\nu = 1.0 \times 10^4$ m^2 s^{-1} and $N_v = 10$. The rate of convergence is slower in this case as compared to the steady-state test case 2, possibly because of the extreme nonlinear nature of the problem due to rough orography. As expected, the LDG model converges monotonically and the convergence is strongly influence by the diffusion coefficient ν.

Next we test the influence of diffusion mechanism in the evolution of relative vorticity fields. We consider the LDG formulation and the ELD used for the discretization of (6) where the interelement contributions are ignored. The model is integrated for 15 (model) days with approximate resolution of 2.5° at the equator ($N_e = 12$, $N_v = 4$). This resolution is comparable to that of a ''T42''

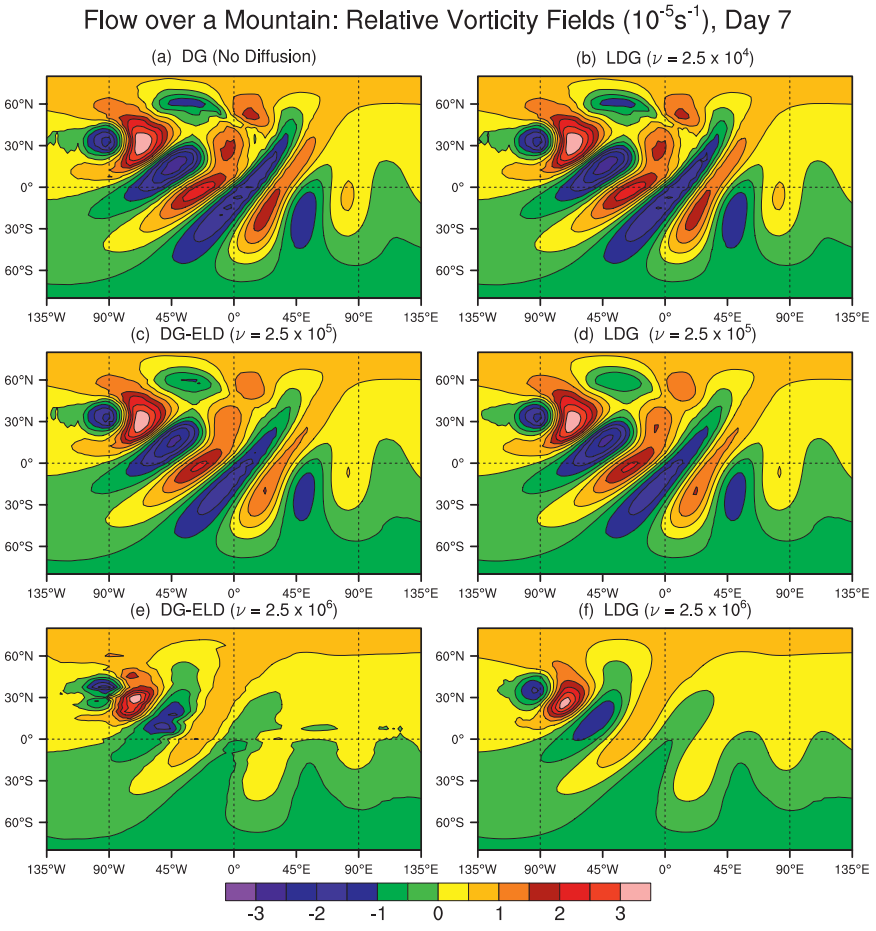

FIG. 5. The relative vorticity field (ζ) at day 7 for the SW test case of flow over an isolated mountain (test case 5). The DG SW model with approximate resolution 2.5° (at the equator) used for this simulation. (a) The vorticity field without diffusion (inviscid flow). The results with ELD with coefficients ν ($m^2\ s^{-1}$) values of (c) 2.5×10^5 and (e) 2.5×10^6. The LDG solution with ν = (b) 2.5×10^4, (d) 2.5×10^5, and (f) 2.5×10^6.

global spectral model. Vorticity fields are initially generated near the mountain and are well developed after 4 days, spreading to the entire domain. Figure 5 shows the relative vorticity fields ($10^{-5}\ s^{-1}$) at day 7 for both LDG and ELD. We have used a set of diffusion coefficients ν with magnitude ranging from *mild* $O(10^4)$ to *strong* $O(10^6)$, for the experiments. Figures 5b,d,f show vorticity fields at model day 7 for the case of LDG method with $\nu = 2.5 \times 10^4\ m^2\ s^{-1}$, $2.5 \times 10^5\ m^2\ s^{-1}$, and $2.5 \times 10^6\ m^2\ s^{-1}$, respectively. The vorticity fields corresponding to ELD are shown in Figs. 5c,e with $\nu = 2.5 \times 10^5\ m^2\ s^{-1}$ and $2.5 \times 10^6\ m^2\ s^{-1}$, respectively. The LDG solutions gradually smooth the vorticity fields and depend on the magnitude of ν.

The vorticity field with ELD for $\nu = 2.5 \times 10^4$ is virtually identical (results not shown) to the nondiffusive case Fig. 5, and with $\nu = 2.5 \times 10^5\ m^2\ s^{-1}$ wiggles are still present at extreme gradients (Fig. 5c). This indicates ELD has a role similar to that of local filter. However, for strong diffusion $\nu = 2.5 \times 10^6\ m^2\ s^{-1}$) the smooth structure of the vorticity fields is completely destroyed (Fig. 5e) as opposed to the LDG case (Fig. 5f). Thus, in the case of ELD the vorticity fields are either slightly smoothed or polluted. This is mainly due to the lack of "communication" (flux exchange) between elementwise locally smoothed fields, when computing the diffusion operator directly. LDG resolves this issue by permitting the exchange of fluxes across the element boundaries for the diffusion terms.

Time traces of the normalized errors for total energy and potential vorticity are shown in Fig. 6 for $\nu = 2.5 \times 10^4\ m^2\ s^{-1}$ and $2.5 \times 10^5\ m^2\ s^{-1}$, and the nondiffused (inviscid) solution is a plotted for a reference. NTL05a provides similar plots for the inviscid case with computational details. In the diffusive case the error growth is at a faster rate and is dependent on the magnitude of ν,

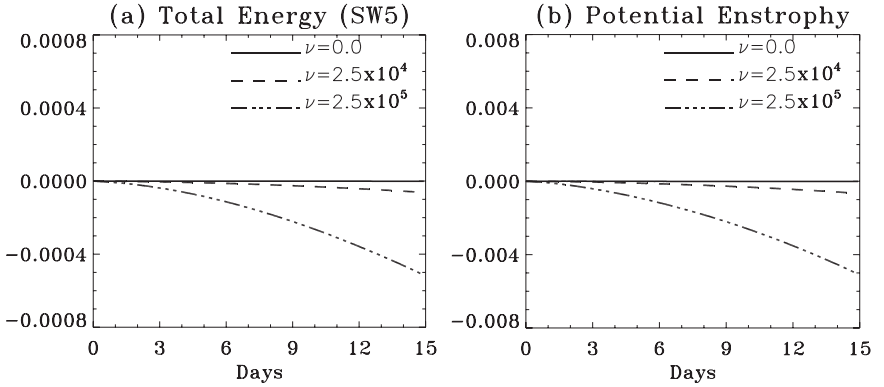

FIG. 6. Time traces of normalized (a) total energy and (b) potential enstrophy for the shallow-water test case 5. The solid lines indicate runs without diffusion, dashed lines show LDG runs with diffusion coefficient $\nu = 2.5 \times 10^4$ m^2 s^{-1}, and the dashed–dotted lines indicate the runs with $\nu = 2.5 \times 10^5$ m^2 s^{-1}. The DG SW model is integrated for 15 days with an approximate resolution of 2.5°.

which is expected for a typical second-order diffusion. Note that the diffusion coefficient ν is a resolution-dependent parameter, and here the choice made for ν is somewhat arbitrary. A judicious choice of ν is possible by looking at the kinetic energy spectra (Collins et al. 2004; Gelb and Gleeson 2001) and is beyond the scope of present work.

c. *Barotropic instability test*

The barotropic instability test proposed by Galewsky et al. (2004) is a challenging test for the SW models developed on the cubed-sphere grids. This test *exposed* artifacts from wavenumber 4 due to the cube-edge discontinuities at low resolutions for various SW models (St-Cyr et al. 2008; Chen and Xiao 2008). The test describes the evolution of a barotropic wave in the Northern Hemisphere and exhibits continuous nonlinear transfer of energy at the midlatitudes from large to small scales. The test is particularly challenging on the cubed-sphere because the vigorous barotropic instability activities are located at the discontinuous edges of the top panel of cubed-sphere grid.

The initial conditions are zonally symmetric and introduce a strong zonal jet along the midlatitudes, and details can be found in Galewsky et al. (2004). The test recommends integrating for 6 days with and without diffusion. Fine features of the vorticity fields can be captured at a resolution about 1.25° or higher (St-Cyr et al. 2008).

To demonstrate the effectiveness of the LDG scheme, the barotropic instability test is run on the cube-sphere grid with approximate resolution of 0.64° ($N_e = 20$, $N_v = 8$). Figure 7 shows the relative vorticity (ζ) fields at day 6 with and without diffusion. The inviscid run is shown in Fig. 7c, where the fine features of the vortex are well captured and comparable to the reference solution given in Fig. 4 of Galewsky et al. (2004). Small-scale noise can be seen at the sharp gradients (Fig. 7c) but at reduced amplitude as compared to the reference solution. A moderate (suboptimal) time step $\Delta t = 6$ s is used for these simulations. The results shown in Figs. 7a,b, respectively, show the LDG runs with $\nu = 1.0 \times 10^5$ m^2 s^{-1} and $\nu = 0.5 \times 10^5$ m^2 s^{-1}. The results shown in Fig. 7a are smooth and comparable to the converged (diffused) reference solution given in Galewsky et al. (2004). LDG successfully eliminates the small-scale noises appearing in Fig. 7c with the appropriate choice of parameter value ν.

5. Conclusions

A second-order diffusion scheme is developed and tested for the discontinuous Galerkin global shallow-water model on the cubed sphere (Nair et al. 2005a). In a nonorthogonal curvilinear coordinate system such as the cubed sphere, the diffusion terms involving Laplacians are more complex and need special treatment. The second-order derivatives present in the diffusion terms prevent using a direct DG discretization of the SW system. So the diffusion scheme developed for the SW model is based on the local discontinuous Galerkin method where the advection–diffusion equation is solved as a first-order system. All of the curvature terms resulting from the cubed-sphere geometry are incorporated into the first-order continuous system. The LDG shallow-water model is based on BR97 formulation where the central flux is used for interelement contributions.

The diffusion scheme is tested with the two standard test cases from W92's test suite, including the steady-state geostrophic flow (with known analytic solution) and zonal flow over an isolated mountain. In addition,

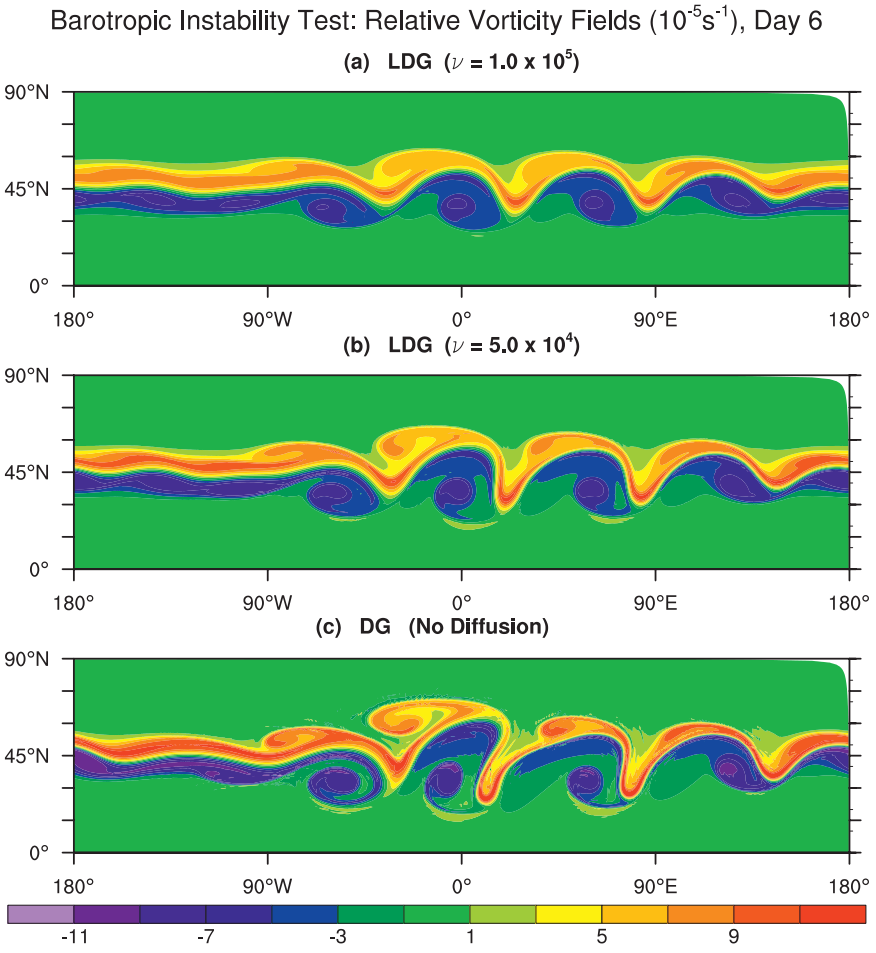

FIG. 7. The relative vorticity field (ζ) at day 6 for the barotropic instability test. The DG SW model with an approximate resolution of 0.64° is used for the simulations. The LDG solution with diffusion coefficient (a) $\nu = 1.0 \times 10^5$ m^2 s^{-1} and (b) 0.5×10^5 m^2 s^{-1}. (c) The inviscid DG solution.

the barotropic instability test proposed by Galewsky et al. (2004) is also considered. The steady-state problem is used for the convergence study, and it is shown that LDG scheme converges monotonically to a diffused state that is influenced by the diffusion coefficient ν. The convergence study is again verified with the zonal flow over the mountain test, and the results are consistent with the previous test.

For the flow over the mountain, LDG can smoothly eliminate small-scale noises, depending on the magnitude of the diffusion coefficient ν. This is evident in the time traces of total energy and potential enstrophy. Moreover, with this test we have demonstrated that an *easy* way of introducing the diffusion operator—by the element-wise localized discretization without incorporating the inter-element contributions—is ineffective or it can even adversely affect the solution. The LDG solution (viscous results) for the barotropic instability test is very similar to the converged reference solution given in Galewsky et al. (2004). The LDG scheme successfully eliminates small-scale noises, and the simulated results are smooth.

The diffusion coefficient (ν) is dependent on the resolution of the model, and our choice for its values in this study is not perfect. However, a judicious choice is possible by looking at the kinetic energy spectra (Collins et al. 2004) and estimating the best physically *accurate* value for ν. The LDG method presented here is an ongoing research effort and will be tested for the HOMME-DG dynamical core (Nair et al. 2009) for idealized climate simulations.

Acknowledgments. I thank Mike Levy, Matt Norman, and Peter Lauritzen for an internal review of this manuscript and Joe Tribbia for a discussion on the diffusion process. I appreciate the helpful comments from two anonymous reviewers, which significantly improved the presentation of the paper. This project is partially

supported by DOE Award DE-FG02-07ER64464. Computer time is provided through the NSF MRI Grants CNS-0421498, CNS-0420873, and CNS-0420985, and through the IBM Shared University Research Program.

REFERENCES

Arnold, D. N., F. Brezzi, B. Cockburn, and L. D. Marini, 2002: Unified analysis of discontinuous Galerkin methods for elliptic problems. *SIAM J. Numer. Anal.,* **39,** 1749–1779.

Bassi, F., and S. Rebay, 1997: A high-order accurate discontinuous finite element method for the numerical solution of the compressible Navier-Stokes equations. *J. Comput. Phys.,* **131,** 267–279.

Burkhardt, U., and E. Becker, 2006: A consistent diffusion-dissipation parameterization in the ECHAM climate model. *Mon. Wea. Rev.,* **134,** 1194–1204.

Chen, C., and F. Xiao, 2008: Shallow water model on cubed-sphere by multi-moment finite volume method. *J. Comput. Phys.,* **227,** 5019–5044.

Cockburn, B., and C.-W. Shu, 1998: The local discontinuous Galerkin for convection diffusion systems. *SIAM J. Numer. Anal.,* **35,** 2440–2463.

——, and ——, 2001: The Runge-Kutta discontinuous Galerkin method for convection-dominated problems. *J. Sci. Comput.,* **16,** 173–261.

Collins, W. D., and Coauthors, 2004: Description of the NCAR Community Atmosphere Model (CAM3.0). NCAR Tech. Note NCAR/TN-464+STR, National Center for Atmospheric Research, Boulder, CO, 226 pp.

Dawson, C., and V. Aizinger, 2002: The local discontinuous Galerkin method for advection-diffusion equations arrising in groundwater and surface water applications. *Inst. Math Appl.,* **131,** 231–242.

Durran, D. R., 1999: *Numerical Methods for Wave Equations in Geophysical Fluid Dynamics*. Springer, 465 pp.

Galewsky, J., L. M. Polvani, and R. K. Scott, 2004: An initial-value problem to test numerical models of the shallow water equations. *Tellus,* **56A,** 429–440.

Gelb, A., and J. P. Gleeson, 2001: Spectral viscosity for shallow water equations in spherical geometry. *Mon. Wea. Rev.,* **129,** 2346–2360.

Giraldo, F. X., and M. Restelli, 2008: A study of spectral element and discontinuous Galerkin methods for the Navier-Stokes equations in nonhydrostatic mesoscale atmospheric modeling: Equation sets and test cases. *J. Comput. Phys.,* **227,** 3849–3877.

Gottlieb, S., C. W. Shu, and E. Tadmor, 2001: Strong stability preserving high-order time discretization methods. *SIAM Rev.,* **43,** 89–112.

Henderson, R. D., 1999: Adaptive spectral element method for turbulance and transition. *High-Order Methods for Computational Physics,* T. J. Barth and H. Deconinck, Eds., Vol. 9, *Lecture Notes in Computational Science and Engineering,* Springer, 225–324.

Karniadakis, G. E., and S. Sherwin, 2005: *Spectral/hp Element Methods for Computational Fluid Dynamics*. Oxford University Press, 686 pp.

Leith, C. E., 1971: Atmospheric predictability and two-dimensional turbulance. *J. Atmos. Sci.,* **28,** 145–161.

Levy, M. N., R. D. Nair, and H. M. Tufo, 2007: High-order Galerkin method for scalable global atmospheric models. *Comput. Geosci.,* **33,** 1022–1035.

Nair, R. D., and H. M. Tufo, 2007: Petascale atmospheric general circulation models. *J. Phys. Conf. Ser.,* **78,** 012078, doi:10.1088/1742-6596/78/1/012078.

——, S. J. Thomas, and R. D. Loft, 2005a: A discontinuous Galerkin global shallow water model. *Mon. Wea. Rev.,* **133,** 876–888.

——, ——, and ——, 2005b: A discontinuous Galerkin transport scheme on the cubed sphere. *Mon. Wea. Rev.,* **133,** 814–828.

——, H.-W. Choi, and H. M. Tufo, 2009: Computational aspects of a scalable high-order discontinuous Galerkin atmospheric dynamical core. *Comput. Fluids,* **38,** 309–319.

Pedlosky, J., 1987: *Geophysical Fluid Dynamics*. 2nd ed. Springer-Verlag, 710 pp.

Persson, P.-O., and J. Peraire, 2006: Sub-cell shock capturing for discontinuous Galerkin methods. *Proc. 44th AIAA Aerospace Science Meeting and Exhibit,* Reno, NV, AIAA, 2006–112.

Sadourny, R., 1972: Conservative finite-difference approximations of the primitive equations on quasi-uniform spherical grids. *Mon. Wea. Rev.,* **100,** 136–144.

Smagorinsky, J., 1963: General circulation experiments with the primitive equations: 1. The basic experiment. *Mon. Wea. Rev.,* **91,** 99–165.

St-Cyr, A., C. Jablonowski, J. M. Dennis, H. M. Tufo, and S. J. Thomas, 2008: A comparison of two shallow water models with nonconforming advaptive grids. *Mon. Wea. Rev.,* **136,** 1898–1922.

Taylor, M., J. Edwards, S. Thomas, and R. Nair, 2007: A mass and energy conserving spectral element atmospheric dynamical core on the cubed-sphere. *J. Phys. Conf. Ser.,* **78,** 012074, doi:10.1088/1742–6596/78/1/012074.

Williamson, D. L., J. B. Drake, J. J. Hack, R. Jakob, and P. N. Swarztrauber, 1992: A standard test set for numerical approximations to the shallow water equations in spherical geometry. *J. Comput. Phys.,* **102,** 211–224.